Letter

Simulating the Haldane model in ultraclean GaAs heterostructures

Francesco Cioni [1,*,†] Lorenzo Cavicchi [2,*] Fabio Taddei [3] and Marco Polini[4]
[1]*NEST, Scuola Normale Superiore, I-56126 Pisa, Italy*
[2]*Scuola Normale Superiore, Piazza dei Cavalieri 7, I-56126 Pisa, Italy*
[3]*Istituto Nanoscienze-CNR, NEST-SNS, Piazza San Silvestro 12, I-56126 Pisa, Italy*
[4]*Dipartimento di Fisica dell'Università di Pisa, Largo Bruno Pontecorvo 3, I-56127 Pisa, Italy*

(Received 25 June 2026; revised 11 October 2026; accepted 22 October 2026; published 9 November 2026)

The Haldane model represents the minimal lattice-based realization of a Chern insulator, exhibiting a quantized Hall conductance in the absence of Landau levels. Despite its conceptual elegance, the implementation in crystalline solids of the requisite pattern of Peierls phases breaking time-reversal symmetry remains experimentally demanding. In this work, we theoretically investigate the possibility to simulate the Haldane model in ultraclean GaAs/AlGaAs heterostructures. Our proposal relies on recent experiments in which a high-mobility two-dimensional electron gas is subject to a gate-defined honeycomb electrostatic potential and a laterally periodic magnetic field generated by patterned ferromagnetic structures. The combined electrostatic and magnetic superlattices furnish a viable route to emulate the topological properties of the Haldane model.

DOI: 10.1103/rk2w-qmk7

Introduction. More than two decades ago, Haldane proposed a minimal lattice model to prove that a quantized Hall response can exist *without* Landau levels [1]. In its canonical formulation on the honeycomb lattice, the model realizes a Chern insulator by combining real nearest-neighbor hopping with complex next-nearest-neighbor tunneling phases that break time-reversal symmetry while maintaining *zero net magnetic flux* per unit cell (UC) [1].

While the Haldane model has been realized experimentally by using cold fermionic gases loaded in honeycomb optical lattices [2], its implementation in a crystalline solid is notoriously challenging [3–6]. The essential requirement is a pattern of effective Peierls phases that breaks time-reversal symmetry on the scale of a UC while keeping the average flux per UC at or close to zero. This condition is generally extremely hard to realize experimentally in a solid-state platform. Consequently, many solid-state realizations of quantized Hall responses at zero applied fields have utilized different microscopic routes, most notably the quantum anomalous Hall effect [7] in magnetically doped topological-insulator thin films [8–11] and multilayer structures consisting of alternating magnetic and undoped topological insulator layers [12,13]. More recently, moiré materials have demonstrated that Chern insulating states can emerge in electrically tunable minibands [14–17], but this typically relies on an emergent band reconstruction driven by strong electron-electron interactions.

Ultraclean GaAs/AlGaAs heterostructures [18,19] offer a complementary route in which the kinetic term of a target lattice Hamiltonian can be imposed externally on an exceptionally low-disorder two-dimensional electron gas (2DEG). A key milestone was the development of so-called "artificial graphene" [20–22] in GaAs quantum wells, where a nanofabricated honeycomb modulation [23–29] produces minibands with graphenelike massless-Dirac-fermion features and enables the exploration of interaction physics in a controllable lattice environment. The central advantage of the GaAs/AlGaAs heterostructure platform is that both geometry and energy scales are engineered at the device level while retaining direct access to standard transport probes.

More recently [30], gate-defined artificial electrostatic crystals in ultra-shallow GaAs quantum wells have pushed this approach toward Hamiltonian engineering. By continuously tuning the modulation strength and carrier density and using DC transport as a probing tool, Wang *et al.* [30] demonstrated the formation of artificial band structures that can be reshaped *in situ*. Different regimes consistent with graphenelike linear (Dirac) dispersion and kagomelike flat-band physics were explored within a *single* device. This level of tunability is difficult to achieve in etched lattices and is particularly relevant for solid-state quantum simulation, where resolving small gaps requires ultralow disorder.

Not only can the honeycomb lattice be engineered lithographically [24–26,29] or electrostatically [20,23,27,28,30], but a controlled breaking of time-reversal symmetry in the orbital sector can be achieved through periodic magnetic-field engineering. In lateral magnetic superlattices, patterned superconducting or ferromagnetic structures placed above the heterostructure generate a spatially modulated perpendicular field $B_z(\boldsymbol{r})$ and, hence, a designed vector potential $\boldsymbol{A}(\boldsymbol{r})$. A seminal demonstration [31] used superconducting stripe arrays to form a lateral magnetic superlattice directly

*These authors contributed equally to this work.
†Contact author: francesco.cioni@sns.it

Published by the American Physical Society under the terms of the Creative Commons Attribution 4.0 International license. Further distribution of this work must maintain attribution to the author(s) and the published article's title, journal citation, and DOI.

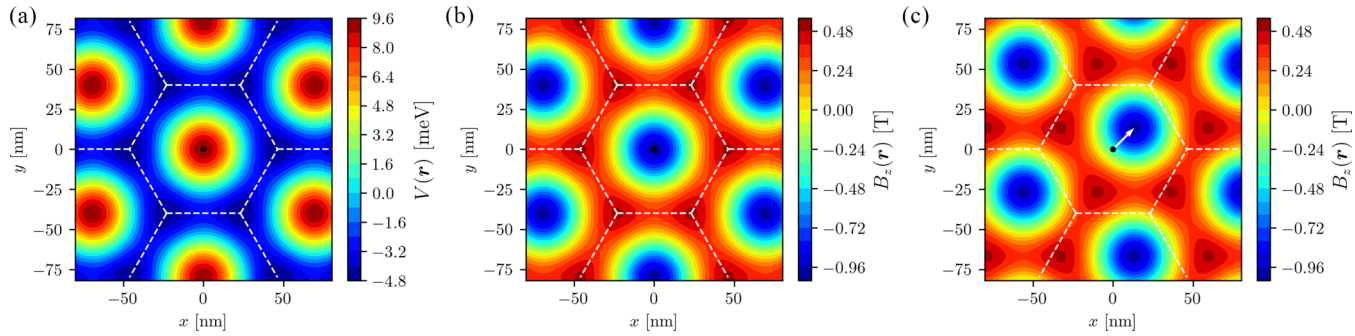


FIG. 1. (a) Crystal field $V(\boldsymbol{r})$ as obtained from Eq. (3). (b) PMF $B_z(\boldsymbol{r})$ as obtained from Eq. (4). (c) PMF shifted by a vector $\boldsymbol{r}_0$ with respect to the crystal field, i.e., $B_z(\boldsymbol{r}-\boldsymbol{r}_0)$. Parameters are fixed to be $a_0 = 80$ nm, $W = 1.57$ meV, and $\beta\Phi_0/2\pi = 330$ mT. In all panels, the black dot in the center of the figure refers to the origin of the axis and is added as a guide for the eye.

coupled to a high-mobility 2DEG. Complementarily, regular arrays of micromagnets [32–34] have been shown to induce periodic magnetic-field modulations at submicron scales in GaAs/AlGaAs heterostructures. When combined with an engineered honeycomb electrostatic potential, such periodic magnetic architectures could provide a physically direct route to break time-reversal symmetry and target flux textures with vanishing flux over a UC. We stress that any unintended uniform magnetic-field component generated by a periodic array of micromagnets can be fully compensated by an external magnetic field of matching strength applied in the opposite direction.

These capabilities make simulating the Haldane model in GaAs/AlGaAs heterostructures a concrete and experimentally relevant possibility. In this work, we address the feasibility of realizing such a quantum simulation platform by studying an artificial honeycomb electrostatic lattice combined with a spatially periodic magnetic field (PMF). We show that the superimposed magnetic pattern can induce a nontrivial topology of the bands, and we map the emerging low-energy physics directly onto the Haldane model. The broader objective is to realize a solid-state quantum simulator for a paradigmatic Chern-insulating Hamiltonian—conceptually simple, yet microscopically elusive in natural crystals—in an experimentally-relevant platform that is tunable and electrically reconfigurable.

Model Hamiltonian. We consider a noninteracting two-dimensional system of spinless electrons subject to a crystalline potential $V(\hat{\boldsymbol{r}})$ and a PMF $\boldsymbol{B}(\hat{\boldsymbol{r}})$. Both fields are periodic with the same lattice periodicity. The magnetic field is chosen such that the net flux through each UC vanishes, which guaranties that the corresponding vector potential $\boldsymbol{A}(\hat{\boldsymbol{r}})$ can be taken to be periodic with the same period as the crystalline potential $V(\hat{\boldsymbol{r}})$. The single-particle Hamiltonian reads

$$\hat{\mathcal{H}} = \frac{1}{2m^*}\left[\hat{\boldsymbol{p}} + \frac{e}{c}\boldsymbol{A}(\hat{\boldsymbol{r}})\right]^2 + V(\hat{\boldsymbol{r}}), \tag{1}$$

where m^* is the effective electron mass ($m^* \simeq 0.062\, m_e$ in GaAs [35], where m_e is the bare electron mass in vacuum), $-e < 0$ is the elementary charge, and c is the speed of light.

For concreteness, we specialize to a triangular lattice. The periodicity of $V(\boldsymbol{r})$ and $\boldsymbol{B}(\boldsymbol{r})$ is set by the primitive vectors

$$\boldsymbol{a}_{1/2} = a_0\left(\pm\frac{\sqrt{3}}{2}, \frac{1}{2}\right), \tag{2}$$

with a_0 the lattice constant. Specifically, we take the crystal potential to be [36]

$$V(\boldsymbol{r}) = 2W\sum_{\ell=1,3,5}\cos(\boldsymbol{G}_\ell\cdot\boldsymbol{r}), \tag{3}$$

and align the PMF along the $\hat{z}$ axis [$\boldsymbol{B}(\boldsymbol{r}) \equiv B_z(\boldsymbol{r})\hat{z}$], setting [37]

$$B_z(\boldsymbol{r}) = \frac{\beta}{2\pi}\Phi_0\sum_{\ell=1,3,5}\cos(\boldsymbol{G}_\ell\cdot\boldsymbol{r}). \tag{4}$$

Here W sets the strength of the crystalline potential, β is a parameter–with the dimensions of an inverse area—controlling the PMF amplitude in units of $\Phi_0/(2\pi)$, $\Phi_0 = hc/e$ being the flux quantum, and

$$\boldsymbol{G}_\ell = \frac{4\pi}{\sqrt{3}a_0}(\cos(\ell\pi/3),\ \sin(\ell\pi/3)) \tag{5}$$

are reciprocal lattice vectors. Since the magnetic field is periodic and carries zero flux per UC, we adopt a periodic (Coulomb) gauge in which $\boldsymbol{\nabla}\cdot\boldsymbol{A}(\boldsymbol{r}) = 0$ and

$$\boldsymbol{A}(\boldsymbol{r}) = \frac{\beta\Phi_0}{2\pi}\sum_{\ell=1,3,5}\frac{\boldsymbol{G}_\ell\wedge\hat{z}}{|\boldsymbol{G}_\ell|^2}\sin(\boldsymbol{G}_\ell\cdot\boldsymbol{r}). \tag{6}$$

Figure 1 displays the spatial profiles of $V(\boldsymbol{r})$ and $B_z(\boldsymbol{r})$ introduced in Eqs. (3) and (4). Figure 1(a) shows that the crystal field generates an array of attractive wells arranged on a D_{6h}-symmetric honeycomb lattice. The PMF configuration depicted in Fig. 1(b) yields a similar spatial structure. To produce the data in Fig. 1, we choose $a_0 = 80$ nm, $m^* = 0.062\, m_e$, and $W = 1.57$ meV, values compatible with experimentally accessible parameters in GaAs heterostructures [30,36]. Unless indicated otherwise, we will employ this parameter set throughout the remainder of this work.

Symmetries. It is known that a periodic magnetic texture with zero net flux aligned with the crystal potential, as in Eq. (6), represents a physical implementation of the Haldane model with vanishing Semenoff mass [1]. In what follows, we

introduce a generalized version of the Haldane Hamiltonian by allowing for a relative displacement $\boldsymbol{r}_0 = (x_0, y_0)$ between the crystal potential and the PMF, as shown in Fig. 1(c). The Hamiltonian of the system thus becomes

$$\hat{\mathcal{H}}(\boldsymbol{A}, \boldsymbol{r}_0) = \frac{1}{2m^*}\left[\hat{\boldsymbol{p}} + \frac{e}{c}\boldsymbol{A}(\hat{\boldsymbol{r}} - \boldsymbol{r}_0)\right]^2 + V(\hat{\boldsymbol{r}}). \tag{7}$$

For any shift vector $\boldsymbol{r}_0$, the Hamiltonian remains invariant under lattice translations. Indeed, the equalities $V(\boldsymbol{r} + \boldsymbol{a}) = V(\boldsymbol{r})$ and $\boldsymbol{A}(\boldsymbol{r} + \boldsymbol{a}) = \boldsymbol{A}(\boldsymbol{r})$, where $\boldsymbol{a} = i\boldsymbol{a}_1 + j\boldsymbol{a}_2$ is a Bravais-lattice translation vector, imply that $[\hat{\mathcal{H}}, \hat{T}_{\boldsymbol{a}}] = 0$, $\hat{T}_{\boldsymbol{a}} \equiv e^{-(i/\hbar)\hat{\boldsymbol{p}}\cdot\boldsymbol{a}}$ being the translation operator. This symmetry allows one to diagonalize $\hat{\mathcal{H}}$ on a hexagonal Wigner-Seitz Brillouin zone (BZ), even though a generic nonzero shift $\boldsymbol{r}_0 \neq \boldsymbol{0}$ of the PMF relative to the crystalline potential $V(\boldsymbol{r})$ breaks the C_{6z} symmetry of the latter. On the other hand, time-reversal symmetry, $\mathcal{T}$, is broken for any $\boldsymbol{r}_0$ when $\beta \neq 0$, i.e., when a finite magnetic field is present.

Let us now consider the parity symmetry operator $\mathcal{P}$, which acts on the PMF, shifted by a generic vector $\boldsymbol{r}_0$ with respect to $V(\boldsymbol{r})$, as follows:

$$\mathcal{P}\, B_z(\hat{\boldsymbol{r}} - \boldsymbol{r}_0)\, \mathcal{P}^\dagger = B_z(-\hat{\boldsymbol{r}} - \boldsymbol{r}_0) = B_z(\hat{\boldsymbol{r}} + \boldsymbol{r}_0). \tag{8}$$

The second equality comes from the explicit form of $B_z(\boldsymbol{r})$ in Eq. (4). Equation (8) shows that parity symmetry trivially holds when $\boldsymbol{r}_0 = \boldsymbol{0}$. Nonetheless, $\mathcal{P}$ is not always broken when $\boldsymbol{r}_0 \neq \boldsymbol{0}$, as can be shown by considering the parity-preserving shift vector $\boldsymbol{r}_0^{\mathrm{p}}$ that satisfies

$$\boldsymbol{G}_1 \cdot \boldsymbol{r}_0^{\mathrm{p}} = n\pi, \qquad \boldsymbol{G}_3 \cdot \boldsymbol{r}_0^{\mathrm{p}} = m\pi, \tag{9}$$

with $n, m \in \mathbb{Z}$. This implies that

$$\boldsymbol{G}_5 \cdot \boldsymbol{r}_0^{\mathrm{p}} = -(\boldsymbol{G}_1 + \boldsymbol{G}_3) \cdot \boldsymbol{r}_0^{\mathrm{p}} = -(n + m)\pi. \tag{10}$$

Using $\boldsymbol{r}_0 = \boldsymbol{r}_0^{\mathrm{p}}$ in the expression of the PMF of Eq. (4) gives

$$\begin{aligned} B_z\big(\boldsymbol{r} - \boldsymbol{r}_0^{\mathrm{p}}\big) = \frac{\beta}{2\pi}\Phi_0[(-1)^n \cos(\boldsymbol{G}_1 \cdot \boldsymbol{r}) + (-1)^m \cos(\boldsymbol{G}_3 \cdot \boldsymbol{r}) \\ + (-1)^{n+m} \cos(\boldsymbol{G}_5 \cdot \boldsymbol{r})], \end{aligned} \tag{11}$$

which is even under parity since it is a superposition of even functions of $\boldsymbol{r}$. In particular, if both n and m are even, the field is explicitly equal to the case $\boldsymbol{r}_0 = \boldsymbol{0}$, and parity holds trivially. The conditions in Eq. (9) are explicitly satisfied by

$$\boldsymbol{r}_0^{\mathrm{p}} = \frac{a_0}{2}\left(-m\frac{\sqrt{3}}{2},\, n + \frac{m}{2}\right). \tag{12}$$

By analogous arguments, the combined parity-time-reversal symmetry ($\mathcal{PT}$), which acts on the Hamiltonian (7) as

$$\begin{aligned} \mathcal{PT}\hat{\mathcal{H}}(\boldsymbol{A}, \boldsymbol{r}_0)\mathcal{P}^\dagger\mathcal{T}^\dagger &= \frac{1}{2m^*}\left[\hat{\boldsymbol{p}} - \frac{e}{c}\boldsymbol{A}(\hat{\boldsymbol{r}} + \boldsymbol{r}_0)\right]^2 + V(\hat{\boldsymbol{r}}) \\ &= \hat{\mathcal{H}}(-\boldsymbol{A}, -\boldsymbol{r}_0), \end{aligned} \tag{13}$$

requires

$$B_z(\boldsymbol{r} - \boldsymbol{r}_0) = -B_z(\boldsymbol{r} + \boldsymbol{r}_0), \quad \forall\, \boldsymbol{r}. \tag{14}$$

It is easy to check that the above equality is never satisfied. This means that there is no vector $\boldsymbol{r}_0$ for which the system is $\mathcal{PT}$ symmetric.

Band structure and topological phase diagram. Using a plane-wave expansion (see Sec. S1 of Supplemental Material (SM) [38]), one can diagonalize $\hat{\mathcal{H}}$ and obtain the band dispersion $\epsilon_{\boldsymbol{k},\lambda}$, where λ represents the band index ($\lambda = 1$ denoting the lowest band). Figure 2 shows three representative band structures for different magnetic-field patterns. Figure 2(a) corresponds to $\beta\Phi_0/(2\pi) = 0$, where Dirac cones appear at K and K'. This is expected because, for the choice of the crystal field in Eq. (3), the electrons experience attractive potential minima arranged on a honeycomb lattice [see Fig. 1(a)]. As shown in Fig. 2(b), a finite magnetic field, $\beta\Phi_0/(2\pi) \simeq 330$ mT (corresponding to $\beta = 1 \times 10^{-3}$ nm^{-2}), opens gaps at both K and K'. Parity remains preserved in this case since $B_z(\boldsymbol{r})$ is aligned with $V(\boldsymbol{r})$, i.e. $\boldsymbol{r}_0 = \boldsymbol{0}$. To break both time-reversal and parity symmetry, one must choose a shift vector $\boldsymbol{r}_0 \notin \{\boldsymbol{0}, \boldsymbol{r}_0^{\mathrm{p}}\}$, $\boldsymbol{r}_0^{\mathrm{p}}$ being given by Eq. (12). Figure 2(c) shows the bands for a representative shift $\boldsymbol{r}_0$ chosen within the UC. Asymmetric gaps open at the Dirac points, which are also displaced away from K and K' due to the broken C_{3z} symmetry. The magnetic field is fixed as in Fig. 2(b).

Figure 3 shows the topological phase diagram [38,39], namely the Chern number $\mathcal{C}$ of the lowest bands $\epsilon_{\boldsymbol{k},\lambda=1}$ as a function of the shift vector $\boldsymbol{r}_0 = (x_0, y_0)$ for two values of the magnetic field—$\beta\Phi_0/(2\pi) = 33$ mT in Fig. 3(a) and $\beta\Phi_0/(2\pi) = 330$ mT in Fig. 3(b). Red regions correspond to $\mathcal{C} = +1$, while blue regions to $\mathcal{C} = -1$. In both cases, the plots show that the presence of a crystal potential yields topologically nontrivial bands and a complex but regular phase diagram controlled by β and $\boldsymbol{r}_0$. In particular, for a small value of magnetic field β, Fig. 3(a), the system is always topologically nontrivial with either red or blue regions. On the other hand, for a higher value of β, Fig. 3(b), the phase diagram also presents trivial regions ($\mathcal{C} = 0$), reported in white. Note that the red and blue regions are separated by isolated gap-closing points, one of which ($\boldsymbol{r}_0^\star$) is marked as a light-green cross. We shall see below that an analogy with the Haldane model can be drawn by introducing a low-energy effective model of the Hamiltonian Eq. (1).

Mapping onto the Haldane model. Projecting onto the subspace of Dirac cones near the K and K' valleys, one can approximate Eq. (1) to first order in the momentum deviation from the Dirac points and to second order in the magnetic-field amplitude β (see Sec. S3 of the SM [38]). The resulting low-energy Hamiltonian is

$$\begin{aligned} H_\tau^{\mathrm{eff}}(\boldsymbol{q}) = \hbar v[\tau(q_y - q_{0,y})\sigma_x + (q_x - q_{0,x})\sigma_y] \\ + (\tau m_{\mathrm{H}} + m_{\mathrm{S}})\,\sigma_z + \tau d_0^{(1)}\mathbb{I} + \mathcal{O}(q^2, \beta^3), \end{aligned} \tag{15}$$

where $\boldsymbol{q}$ denotes a small deviation from K or K', $\tau = \pm 1$ labels the valley, and $\sigma_{i=x,y,z}$ are Pauli matrices acting in the sublattice space. Remarkably, and apart from the vector $\boldsymbol{q}_0 \equiv (q_{0,x}, q_{0,y})$ that originates from the breaking of C_{3z} symmetry induced by a finite $\boldsymbol{r}_0 \neq \boldsymbol{0}$ displacement, Eq. (15) coincides

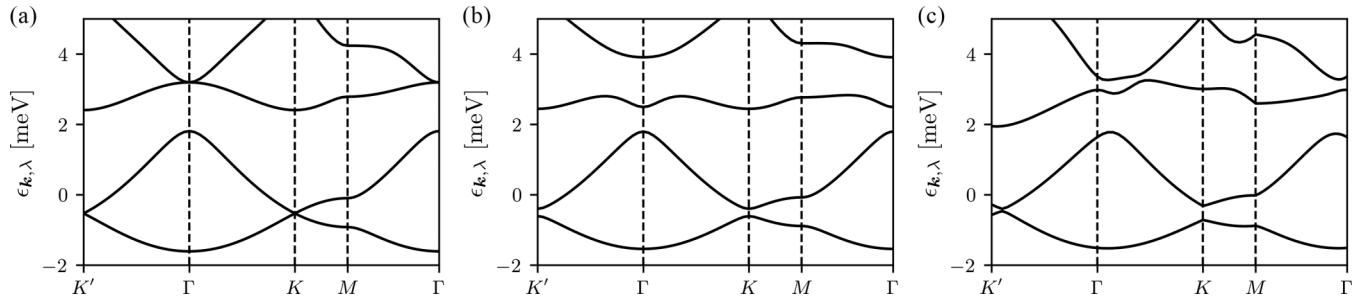


FIG. 2. Energy bands, along the high-symmetry path $K' - \Gamma - K - M - \Gamma$ in the BZ, for different magnetic-field patterns. (a) $\beta\Phi_0/2\pi = 0$ and $\boldsymbol{r}_0 = \boldsymbol{0}$. (b) $\beta\Phi_0/2\pi = 330$ mT and $\boldsymbol{r}_0 = \boldsymbol{0}$. (c) $\beta\Phi_0/2\pi = 330$ mT and $\boldsymbol{r}_0 = a_0(-0.45, -0.43)$. Other parameters are chosen as $a_0 = 80$ nm, $m^* = 0.062\, m_e$, and $W = 1.57$ meV.

with the low-energy expansion of the Haldane model around K and K' (see Ref. [40]). Such a mapping onto the Haldane model, though, has the peculiarity that m_{H} (the Haldane mass) and m_{S} (the Semenoff mass) are not independent quantities.

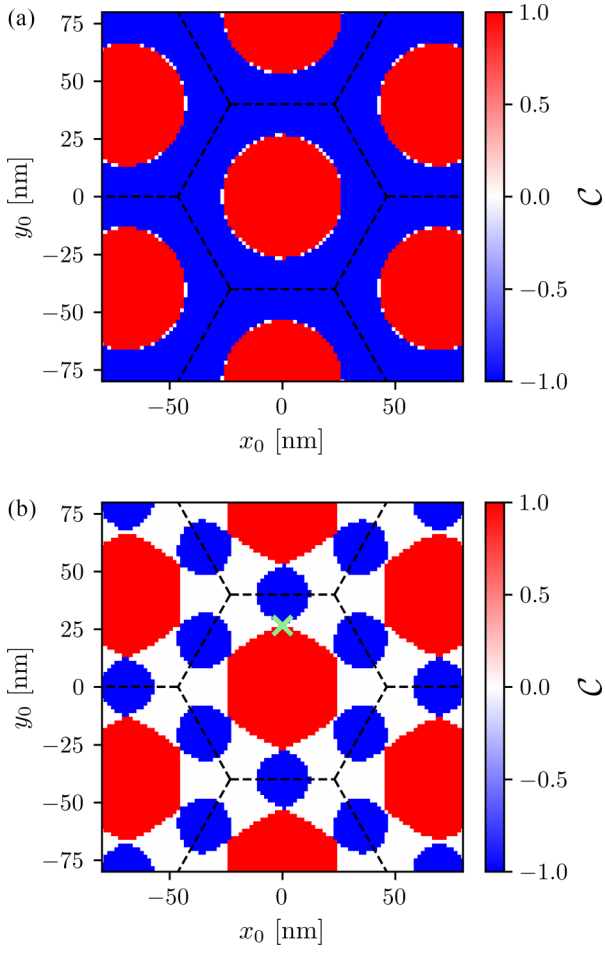


FIG. 3. Topological phase diagram. The Chern number $\mathcal{C}$ of the lowest band $\epsilon_{\boldsymbol{k},\lambda=1}$ as a function of the shift vector $\boldsymbol{r}_0 = (x_0, y_0)$. (a) $\beta\Phi_0/(2\pi) = 33$ mT. (b) $\beta\Phi_0/(2\pi) = 330$ mT. All other parameters are fixed as in Fig. 2. The light-green cross marks the gap-closing point $\boldsymbol{r}_0^\star$. The dashed black lines outline the hexagonal UC of the direct lattice.

Such masses, in fact, are expressed in terms of the microscopic parameters of Eq. (1) as [38]

$$m_{\mathrm{H}} = -\frac{\sqrt{3}t_1}{3}\beta \sum_{\ell=1,3,5} \cos(\boldsymbol{G}_\ell \cdot \boldsymbol{r}_0), \tag{16a}$$

$$m_{\mathrm{S}} = \frac{\sqrt{3}}{3}\left[t_2 + \frac{t_1^2}{9W}\right]\beta^2 \sum_{\ell=1,3,5} \sin(\boldsymbol{G}_\ell \cdot \boldsymbol{r}_0) - \frac{4\sqrt{3}\,t_1^2}{27W}\beta^2 \prod_{\ell=1,3,5} \sin(\boldsymbol{G}_\ell \cdot \boldsymbol{r}_0), \tag{16b}$$

where $t_1 \equiv \frac{e\hbar}{m^* c}\frac{\Phi_0}{8\pi\sqrt{3}}$ and $t_2 \equiv \frac{e^2}{8m^* c^2 G^2}(\frac{\Phi_0}{2\pi})^2$. Both depend nontrivially on $\boldsymbol{r}_0$ and β. Equations (16a) and (16b) show that while m_{H} is linear in β and remains finite in the limit $\boldsymbol{r}_0 = \boldsymbol{0}$, m_{S} is quadratic in β and vanishes when $\boldsymbol{r}_0 = \boldsymbol{0}$. Haldane mass and Semenoff mass are plotted in Figs. 4(a) and 4(b), respectively, as functions of x_0 and y_0.

Note that the Chern number calculated from the Haldane expression $\mathcal{C} = \frac{1}{2}[\mathrm{sgn}(m_{\mathrm{S}} - m_{\mathrm{H}}) - \mathrm{sgn}(m_{\mathrm{S}} + m_{\mathrm{H}})]$, using Eqs. (16a) and (16b), coincides with the plot in Fig. 3(a), obtained with the full model Hamiltonian (1).

Interestingly, it turns out that the two masses can be tuned independently around some specific points $\boldsymbol{r}_0$. We first note that both m_{H} and m_{S} vanish at the gap-closing point $\boldsymbol{r}_0^\star = \frac{1}{3}(\boldsymbol{a}_1 + \boldsymbol{a}_2)$, marked by the dark green cross in Fig. 4 and corresponding to the light-green cross shown in Fig. 3. Considering the region in the vicinity of $\boldsymbol{r}_0^\star$, we also note that m_{H} and m_{S} remain zero along orthogonal directions (tangent to the white circle for m_{H} and along the vertical axis for m_{S}). This implies that the two masses can be tuned independently in the neighborhood of $\boldsymbol{r}_0^\star$, thus allowing to access a broader phase diagram. The same behavior holds for the other gap-closing points, obtained from $\boldsymbol{r}_0^\star$ by C_{6z} rotations around the origin.

To make this argument quantitative, we use the approximate expressions (16a) and (16b) and expand m_{H} and m_{S} about $\boldsymbol{r}_0^\star$. Let

$$\delta\boldsymbol{r} \equiv \boldsymbol{r}_0 - \boldsymbol{r}_0^\star, \tag{17}$$

and define unit vectors that are parallel and perpendicular to $\boldsymbol{r}_0^\star$ (see Fig. 4),

$$\hat{\boldsymbol{e}}_\parallel \equiv \frac{\boldsymbol{r}_0^\star}{|\boldsymbol{r}_0^\star|}, \qquad \hat{\boldsymbol{e}}_\perp \text{ such that } \hat{\boldsymbol{e}}_\perp \cdot \hat{\boldsymbol{e}}_\parallel = 0, \tag{18}$$

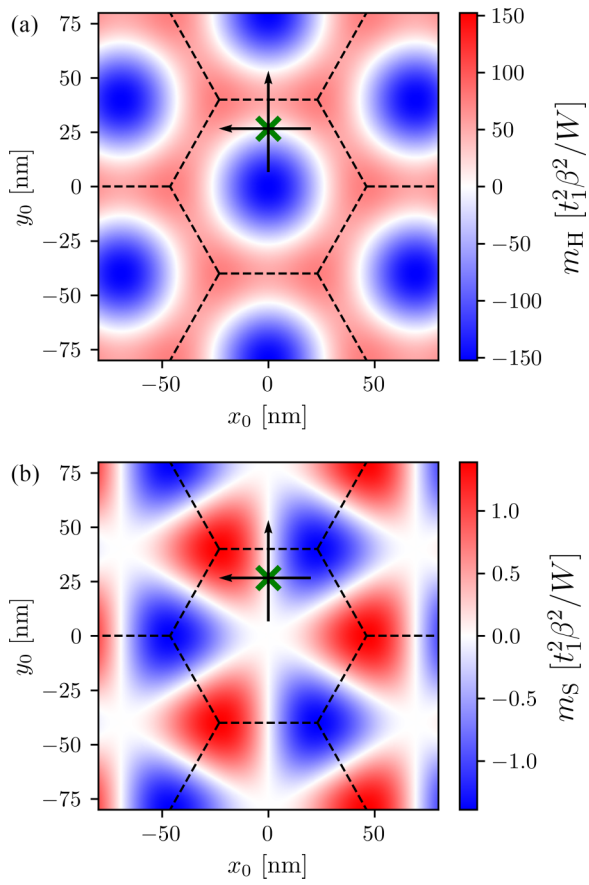


FIG. 4. (a) Haldane mass m_H from Eq. (16a). (b) Semenoff mass m_S from Eq. (16b). For comparison, we express both masses in units of the energy $t_1^2\beta^2/W$. The dark green cross marks the gap-closing point $\boldsymbol{r}_0^\star$, and the axes indicate the decoupling directions $\hat{\boldsymbol{e}}_\parallel$ and $\hat{\boldsymbol{e}}_\perp$. Here we fixed $\beta\Phi_0/(2\pi) = 33$ mT. All other parameters are fixed as in Fig. 2.

so that

$$\delta\boldsymbol{r} = \delta_\parallel\,\hat{\boldsymbol{e}}_\parallel + \delta_\perp\,\hat{\boldsymbol{e}}_\perp. \tag{19}$$

Expanding the Haldane mass (16a) in $\delta\boldsymbol{r}$ yields

$$m_H(\boldsymbol{r}_0^\star + \delta\boldsymbol{r}) = \frac{2\pi t_1}{a_0}\,\beta\,\delta_\parallel + \mathcal{O}(\delta_\parallel^2, \delta_\perp^2), \tag{20}$$

the leading term being $\mathcal{O}(\delta_\parallel)$. In particular, notice that there is no linear dependence on $\delta_\perp$.

Expanding the Semenoff mass (16b) up to first order in $\delta\boldsymbol{r}$, one finds

$$m_S(\boldsymbol{r}_0^\star + \delta\boldsymbol{r}) = \frac{2\pi}{a_0}\left(t_2 + \frac{t_1^2}{9W}\right)\beta^2\,\delta_\perp + \mathcal{O}(\delta_\perp^2, \delta_\parallel\delta_\perp), \tag{21}$$

with no linear dependence on $\delta_\parallel$. Equations (20) and (21) show that, in a neighborhood of $\boldsymbol{r}_0^\star$, the Haldane and Semenoff masses are locally decoupled at linear order. Hence, for shifts $\boldsymbol{r}_0$ sufficiently close to $\boldsymbol{r}_0^\star$, the independent control parameters $\delta_\parallel$ and $\delta_\perp$ tune the valley-odd and valley-even mass components separately at leading order. Furthermore, consider a vertical cut through the point $\boldsymbol{r}_0^\star = \frac{1}{3}(\boldsymbol{a}_1 + \boldsymbol{a}_2)$ in the phase diagram of Fig. 3(b). The resulting profile closely resembles the Haldane phase diagram at $\varphi = \pi$ [1], which separates the $\mathcal{C} = -1$ phase from the $\mathcal{C} = 1$ phase. Remarkably, this shows that even for arbitrary values of the PMFs, we find a direct analogy with the Haldane model by focusing on regions of the phase diagram around the gap-closing points.

Summary and conclusions. We studied a minimal model of spinless, noninteracting electrons in two spatial dimensions subject to a periodic scalar potential $V(\boldsymbol{r})$ and a PMF $B_z(\boldsymbol{r})$ with zero net flux per UC. The vanishing-flux condition allows for a periodic gauge and preserves ordinary lattice translations for any relative displacement $\boldsymbol{r}_0$ between the two patterns $V(\boldsymbol{r})$ and $B_z(\boldsymbol{r})$, providing topological Bloch bands without a uniform magnetic field.

Numerical plane-wave diagonalization shows that the PMF opens gaps at the Dirac points of the underlying honeycomb-like low-energy structure and generates extended regions of nonzero Chern number. The resulting topological phase diagram is controlled by the field amplitude β and by the shift $\boldsymbol{r}_0$.

A low-energy projection near K and K' maps the model onto a Haldane-type massive Dirac theory with a valley-odd Haldane mass m_H and a valley-even Semenoff mass m_S. Microscopically, m_H appears at $\mathcal{O}(\beta)$, whereas m_S arises at $\mathcal{O}(\beta^2)$ and vanishes as $\boldsymbol{r}_0 \to \boldsymbol{0}$, explaining the weak-field phase boundaries dominated by $m_H = 0$ and the stronger-field topological properties induced by m_S. Although the two masses are generally linked functions of $(\beta, \boldsymbol{r}_0)$, near special gap-closing points $\boldsymbol{r}_0^\star$, they decouple to linear order, such that orthogonal displacements independently tune m_H and m_S, recovering the canonical Haldane control parameters locally.

These results identify the relative shift $\boldsymbol{r}_0$ between the periodic scalar potential $V(\boldsymbol{r})$ and the PMF $B_z(\boldsymbol{r})$ as a purely geometric knob to switch between Chern phases and to engineer chiral edge physics in experimentally relevant parameter ranges. From an experimental perspective, we believe that the main challenge will be to integrate the electrostatic and magnetic superlattices while controlling the spatially averaged magnetic field at the position of the 2DEG. Concerning possible experimental implementations, we also stress that the choice of PMF considered here is only one example leading to topologically nontrivial phases. Indeed, as shown in the SM [38], a different choice of PMF yields a phase diagram with extended regions of nonzero Chern number. Extensions to include spin, interactions, and disorder will clarify the robustness of our results and are left for future work.

Acknowledgments. It is a pleasure to thank O. Sushkov and A. Hamilton for useful discussions. M.P. was supported by the European Union under Grant Agreement No. 101131579 - Exqiral. F.T. acknowledges funding from MUR-PRIN 2022 - Grant No. 2022B9P8LN - (PE3)- Project NEThEQS "Non-equilibrium coherent thermal effects in quantum systems" in PNRR Mission 4 - Component 2 - Investment 1.1 "Fondo per il Programma Nazionale di Ricerca e Progetti di Rilevante Interesse Nazionale (PRIN)" funded by the European Union - Next Generation EU, and from the Royal Society through the International Exchanges between the United Kingdom and Italy (Grant No. IEC R2 212041).

Views and opinions expressed are however those of the author(s) only and do not necessarily reflect those of the European Union or the European Commission. Neither the European Union nor the granting authority can be held responsible for them.

Data availability. There are no publicly available research data or software supporting this manuscript. Requests for further information or data should be sent to the authors.

[1] F. D. M. Haldane, Model for a quantum Hall effect without Landau levels: Condensed-matter realization of the "parity anomaly", Phys. Rev. Lett. **61**, 2015 (1988).

[2] G. Jotzu, M. Messer, R. Desbuquois, M. Lebrat, T. Uehlinger, D. Greif, and T. Esslinger, Experimental realization of the topological Haldane model with ultracold fermions, Nature (London) **515**, 237 (2014).

[3] X.-L. Qi and S.-C. Zhang, Topological insulators and superconductors, Rev. Mod. Phys. **83**, 1057 (2011).

[4] A. Wright, Realising Haldane's vision for a Chern insulator in buckled lattices, Sci. Rep. **3**, 2736 (2013).

[5] H.-S. Kim and H.-Y. Kee, Realizing Haldane model in Fe-based honeycomb ferromagnetic insulators, npj Quant. Mater **2**, 20 (2017).

[6] Y.-H. Ho, E. V. Castro, and M. A. Cazalilla, Haldane model under nonuniform strain, Phys. Rev. B **96**, 155446 (2017).

[7] N. Nagaosa, J. Sinova, S. Onoda, A. H. MacDonald, and N. P. Ong, Anomalous Hall effect, Rev. Mod. Phys. **82**, 1539 (2010).

[8] R. Yu, W. Zhang, H.-J. Zhang, S.-C. Zhang, X. Dai, and Z. Fang, Quantized anomalous Hall effect in magnetic topological insulators, Science **329**, 61 (2010).

[9] C.-Z. Chang, J. Zhang, X. Feng, J. Shen, Z. Zhang, M. Guo, K. Li, Y. Ou, P. Wei, L.-L. Wang, Z.-Q. Ji, Y. Feng, S. Ji, X. Chen, J. Jia, X. Dai, Z. Fang, S.-C. Zhang, K. He, Y. Wang, *et al.*, Experimental observation of the quantum anomalous Hall effect in a magnetic topological insulator, Science **340**, 167 (2013).

[10] C.-Z. Chang, W. Zhao, D. Y. Kim, H. Zhang, B. A. Assaf, D. Heiman, S.-C. Zhang, C. Liu, M. H. W. Chan, and J. S. Moodera, High-precision realization of robust quantum anomalous Hall state in a hard ferromagnetic topological insulator, Nat. Mater. **14**, 473 (2015).

[11] Y. Deng, Y. Yu, M. Z. Shi, Z. Guo, Z. Xu, J. Wang, X. H. Chen, and Y. Zhang, Quantum anomalous Hall effect in intrinsic magnetic topological insulator $MnBi_2Te_4$, Science **367**, 895 (2020).

[12] Y.-F. Zhao, R. Zhang, R. Mei, L.-J. Zhou, H. Yi, Y.-Q. Zhang, J. Yu, R. Xiao, K. Wang, N. Samarth, M. H. W. Chan, C.-X. Liu, and C.-Z. Chang, Tuning the Chern number in quantum anomalous Hall insulators, Nature (London) **588**, 419 (2020).

[13] Y.-F. Zhao, R. Zhang, J. Cai, D. Zhuo, L.-J. Zhou, Z.-J. Yan, M. H. W. Chan, X. Xu, and C.-Z. Chang, Creation of chiral interface channels for quantized transport in magnetic topological insulator multilayer heterostructures, Nat. Commun. **14**, 770 (2023).

[14] A. L. Sharpe, E. J. Fox, A. W. Barnard, J. Finney, K. Watanabe, T. Taniguchi, M. A. Kastner, and D. Goldhaber-Gordon, Emergent ferromagnetism near three-quarters filling in twisted bilayer graphene, Science **365**, 605 (2019).

[15] M. Serlin, C. L. Tschirhart, H. Polshyn, Y. Zhang, J. Zhu, K. Watanabe, T. Taniguchi, L. Balents, and A. F. Young, Intrinsic quantized anomalous Hall effect in a moiré heterostructure, Science **367**, 900 (2020).

[16] G. Chen, A. L. Sharpe, E. J. Fox, Y.-H. Zhang, S. Wang, L. Jiang, B. Lyu, H. Li, K. Watanabe, T. Taniguchi, Z. Shi, T. Senthil, D. Goldhaber-Gordon, Y. Zhang, and F. Wang, Tunable correlated Chern insulator and ferromagnetism in a moiré superlattice, Nature (London) **579**, 56 (2020).

[17] W. Zhao, K. Kang, Y. Zhang, P. Knüppel, Z. Tao, L. Li, C. L. Tschirhart, E. Redekop, K. Watanabe, T. Taniguchi, A. F. Young, J. Shan, and K. F. Mak, Realization of the Haldane Chern insulator in a moiré lattice, Nat. Phys. **20**, 275 (2024).

[18] M. J. Manfra, Molecular beam epitaxy of ultra-high-quality AlGaAs/GaAs heterostructures: Enabling physics in low-dimensional electronic systems, Annu. Rev. Condens. Matter Phys. **5**, 347 (2014).

[19] Y. J. Chung, K. A. V. Rosales, K. W. Baldwin, P. T. Madathil, K. W. West, M. Shayegan, and L. N. Pfeiffer, Ultra-high-quality two-dimensional electron systems, Nat. Mater. **20**, 632 (2021).

[20] C.-H. Park and S. G. Louie, Making massless Dirac fermions from a patterned two-dimensional electron gas, Nano Lett. **9**, 1793 (2009).

[21] M. Gibertini, A. Singha, V. Pellegrini, M. Polini, G. Vignale, A. Pinczuk, L. N. Pfeiffer, and K. W. West, Engineering artificial graphene in a two-dimensional electron gas, Phys. Rev. B **79**, 241406(R) (2009).

[22] M. Polini, F. Guinea, M. Lewenstein, H. C. Manoharan, and V. Pellegrini, Artificial honeycomb lattices for electrons, atoms and photons, Nat. Nanotechnol. **8**, 625 (2013).

[23] A. Soibel, U. Meirav, D. Mahalu, and H. Shtrikman, Fabrication and transport measurements of honeycomb surface superlattices, Semicond. Sci. Technol. **11**, 1756 (1996).

[24] D. Scarabelli, S. Wang, A. Pinczuk, S. J. Wind, Y. Y. Kuznetsova, L. N. Pfeiffer, K. West, G. C. Gardner, M. J. Manfra, and V. Pellegrini, Fabrication of artificial graphene in a GaAs quantum heterostructure, J. Vac. Sci. Technol. B **33**, 06FG03 (2015).

[25] S. Wang, D. Scarabelli, Y. Y. Kuznetsova, S. J. Wind, A. Pinczuk, V. Pellegrini, M. J. Manfra, G. C. Gardner, L. N. Pfeiffer, and K. W. West, Observation of electron states of small period artificial graphene in nanopatterned GaAs quantum wells, Appl. Phys. Lett. **109**, 113101 (2016).

[26] S. Wang, D. Scarabelli, L. Du, Y. Y. Kuznetsova, L. N. Pfeiffer, K. W. West, G. C. Gardner, M. J. Manfra, V. Pellegrini, S. J. Wind, and A. Pinczuk, Observation of Dirac bands in artificial graphene in small-period nanopatterned GaAs quantum wells, Nat. Nanotechnol. **13**, 29 (2018).

[27] L. Du, Z. Liu, S. Wind, V. Pellegrini, K. West, S. Fallahi, L. Pfeiffer, M. Manfra, and A. Pinczuk, Observation of flat bands in gated semiconductor artificial graphene, Phys. Rev. Lett. **126**, 106402 (2021).

[28] G. De Simoni, A. Singha, M. Gibertini, B. Karmakar, M. Polini, V. Piazza, L. N. Pfeiffer, K. W. West, F. Beltram, and

V. Pellegrini, Delocalized-localized transition in a semiconductor two-dimensional honeycomb lattice, Appl. Phys. Lett. **97**, 132113 (2010).

[29] A. Singha, M. Gibertini, B. Karmakar, S. Yuan, M. Polini, G. Vignale, M. I. Katsnelson, A. Pinczuk, L. N. Pfeiffer, K. W. West, and V. Pellegrini, Two-dimensional Mott-Hubbard electrons in an artificial honeycomb lattice, Science **332**, 1176 (2011).

[30] D. Q. Wang, Z. Krix, O. A. Tkachenko, V. A. Tkachenko, C. Chen, I. Farrer, D. A. Ritchie, O. P. Sushkov, A. R. Hamilton, and O. Klochan, Correlated insulator in the kagome flat band of a two-dimensional electrostatic crystal, Nat. Phys. **22** 1079 (2026).

[31] H. A. Carmona, A. K. Geim, A. Nogaret, P. C. Main, T. J. Foster, M. Henini, S. P. Beaumont, and M. G. Blamire, Two dimensional electrons in a lateral magnetic superlattice, Phys. Rev. Lett. **74**, 3009 (1995).

[32] P. D. Ye, D. Weiss, R. R. Gerhardts, M. Seeger, K. von Klitzing, K. Eberl, and H. Nickel, Electrons in a periodic magnetic field induced by a regular array of micromagnets, Phys. Rev. Lett. **74**, 3013 (1995).

[33] A. Nogaret, Electron dynamics in inhomogeneous magnetic fields, J. Phys.: Condens. Matter **22**, 253201 (2010).

[34] J. N. Engdahl, A. C. Keser, T. Schmidt, and O. P. Sushkov, Driving viscous hydrodynamics in bulk electron flow in graphene using micromagnets, Phys. Rev. B **109**, 195402 (2024).

[35] P. M. T. Vianez, Y. Jin, W. K. Tan, Q. Liu, J. P. Griffiths, I. Farrer, D. A. Ritchie, O. Tsyplyatyev, and C. J. B. Ford, Decoupling of the many-body effects from the electron mass in GaAs by means of reduced dimensionality, Phys. Rev. B **107**, 115128 (2023).

[36] Z. E. Krix, H. D. Scammell, and O. P. Sushkov, Correlated physics in an artificial triangular anti-dot lattice, Phys. Rev. B **105**, 075120 (2022).

[37] M. Taillefumier, V. K. Dugaev, B. Canals, C. Lacroix, and P. Bruno, Chiral two-dimensional electron gas in a periodic magnetic field: Persistent current and quantized anomalous Hall effect, Phys. Rev. B **78**, 155330 (2008).

[38] See Supplemental Material at http://link.aps.org/supplemental/10.1103/rk2w-qmk7 for more details on the plane-wave expansion method used to diagonalize the Hamiltonian of Eq (1), the calculation of the Chern number, the detailed K-point three-plane-wave expansion used to derive the low-energy Hamiltonian of Eq (15), and results concerning the topological phase diagram for different periodic magnetic field patterns.

[39] T. Fukui, Y. Hatsugai, and H. Suzuki, Chern numbers in discretized Brillouin zone: Efficient method of computing (spin) Hall conductances, J. Phys. Soc. Jpn. **74**, 1674 (2005).

[40] B. A. Bernevig and T. L. Hughes, *Topological Insulators and Superconductors* (Princeton University Press, Princeton, 2013).